Click Here
for
Full
Article

Ross Sea polynyas: Response of ice concentration retrievals to large areas of thin ice

R. Kwok,[1] J. C. Comiso,[2] S. Martin,[3] and R. Drucker[3]

[1] For a 3-month period between May and July of 2005, we examine the response of the Advanced Microwave Scanning Radiometer (AMSR-E) Enhanced NASA Team 2 (NT2) and AMSR-E Bootstrap (ABA) ice concentration algorithms to large areas of thin ice of the Ross Sea polynyas. Coincident Envisat Synthetic Aperture Radar (SAR) coverage of the region during this period offers a detailed look at the development of the polynyas within several hundred kilometers of the ice front. The high-resolution imagery and derived ice motion fields show bands of polynya ice, covering up to ~105 km^2 of the Ross Sea, that are associated with wind-forced advection. In this study, ice thickness from AMSR-E 36 GHz polarization information serves as the basis for examination of the response. The quality of the thickness of newly formed sea ice (<10 cm) from AMSR-E is first assessed with thickness estimates derived from ice surface temperatures from the Moderate Resolution Imaging Spectroradiometer (MODIS) instrument. The effect of large areas of thin ice in lowering the ice concentration estimates from both NT2/ABA approaches is clearly demonstrated. Results show relatively robust relationships between retrieved ice concentrations and thin ice thickness estimates that differ between the two algorithms. These relationships define the approximate spatial coincidence of ice concentration and thickness isopleths. Using the 83% (ABA) and 91% (NT2) isopleths as polynya boundaries, we show that the computed coverage compares well with that using the estimated 10-cm thickness contour. The thin ice response characterized here suggests that in regions with polynyas, the retrieval results could be used to provide useful geophysical information, namely thickness and coverage.

1. Introduction

[2] Even though the spatial resolution is fairly coarse, the great strength of the satellite passive microwave ice concentration records is its coverage and the length of the data record. For the combination of the Scanning Multichannel Microwave Radiometer (SMMR) and the Special Sensor Microwave/Imager (SSM/I), this spans over 25 years. The gridded fields of ice concentration from the Bootstrap (BBA) and NASA Team (NT) algorithms have contributed to a multidecade record that highlights the decline in Arctic Ocean sea ice coverage [*Parkinson et al.*, 1999; *Comiso*, 2002] and the need for understanding the role of sea ice in polar and global climates.

[3] Since the May 2002 launch of the Advanced Microwave Scanning Radiometer-EOS (AMSR-E) on the Aqua platform, improved observations of the Arctic and Antarctic sea ice cover have been acquired. These data are expected to set new directions for polar climate data sets and to provide a baseline for evaluation of the quality and consistency of historical satellite records. With the combined capability of SMMR and SSM/I, the AMSR-E instrument measures vertically and horizontally polarized radiances at 6.9, 10.6, 18.7, 23.8, 36.5, and 89.0 GHz at double the SSM/I spatial resolution [*Comiso et al.*, 2003]. The Enhanced NASA Team (NT2) and AMSR-E Bootstrap (ABA) sea ice algorithms employed for the new data set take advantage of the added channels and better resolution to produce fields of sea ice concentration. The NT2 algorithm uses the 89-GHz channels to correct for atmospheric effects and to reduce anomalies due to surface snow layering, particularly in the Antarctic, present in the lower frequency horizontally polarized data. The ABA uses the 6.9-GHz channels to reduce uncertainties in ice concentration retrieval due to temperature effects that may be associated with extremely cold surface ice conditions (with little or no snow cover). More detailed discussions of these algorithmic improvements are given by *Comiso et al.* [2003] and *Markus and Cavalieri* [2000]. The efficacy of these refinements is currently being

---

[1]Jet Propulsion Laboratory, California Institute of Technology, Pasadena, California, USA.
[2]Cryospheric Sciences Branch, NASA Goddard Space Flight Center, Greenbelt, Maryland, USA.
[3]School of Oceanography, University of Washington, Seattle, Washington, USA.

validated through various studies and field programs [*Meier et al.*, 2004].

[4] This paper focuses on the response of these ice concentration algorithms to relatively large homogeneous areas of young and thin ice compared to the spatial resolution of these instruments. The results of this assessment should find applicability in the interpretation of ice concentration retrievals over active polynyas (areas of combined open water and thin ice). *Martin et al.* [2004] argue that given the rapid formation of frazil and pancake ice with distance downwind from the coast, it is physically more realistic to consider polynyas as containing primarily thin ice with limited open water rather than as primarily open water. From a remote sensing perspective, thin ice has an emissivity signature that lies between the values for open water and those of first-year ice. At 37 GHz and for ice thicknesses greater than ∼50 mm, the high reflectivity of the underlying water no longer contributes to the emitted radiation and subsequent emissivity changes at greater thicknesses arise primarily from changes in the distribution of brine in the uppermost ice layers [*Grenfell et al.*, 1992]. In fact, recent work by *Martin et al.* [2004] used these emissivity changes to determine the thickness of thin ice formed in polynyas. In satellite passive microwave ice concentration retrievals, because of the coarse resolution of current instruments, low concentrations of thin ice are difficult to identify and can be easily confused with mixtures of thick ice and open water. Conversely, large areas of thin ice with very little open water can be interpreted as areas of lower ice concentration. Observed increases in satellite retrievals of ice concentration are due to a combination of changes due to ice growth and to increasing ice concentration. Thus a better understanding of these retrievals would improve their utility in the remote sensing of large polynyas.

[5] Our approach in the characterization of the thin ice response is to examine the empirical relationship between the retrieved ice concentration, C, and thin ice thickness estimates, h, (i.e., $C = f(h)$) at two sites: the Ross Sea Polynya (RSP) and the Terra Nova Bay Polynya (TNB). The RSP, which forms in the Ross Sea to the east of Ross Island and adjacent to the Ross Ice Shelf (RIS) is the largest Antarctic polynya. These regions are ideal for the present analysis: the mean winter coverage of the RSP is about 25,000 km^2 and the TNB is about 3000 km^2 [*Martin et al.*, 2007]. At the AMSR-E spatial footprint, these polynyas provide a large number of homogeneous thin ice areas that are formed under similar conditions. Our approach is as follows. First, we use the ice thickness derived from MODIS ice surface temperature (IST) to assess the robustness of the suggested relationship between thin ice thickness and the 36 GHz V/H ratios [*Martin et al.*, 2004]. As clouds and the water vapor released from the polynya obscure the surface in the visible/infrared, only MODIS retrievals from clear days are used. Then we use the AMSR-derived ice thickness estimates to examine the interpretation of retrieved ice concentration within winter polynyas over three winter months in 2005. Use of the AMSR-E 36 GHz V/H versus thin ice thickness (0–10 cm) relationship is less restrictive than the use of MODIS because this passive microwave channel is relatively unaffected by the atmospheric ice and moisture.

[6] Section 2 describes the data set used in the analyses. Our assessment is restricted to the period from May through July 2005 for which we have near coincident Envisat, MODIS, and AMSR-E data. Section 3 describes the character of the Ross Sea polynyas during a 3-week period in June 2005 for which high-resolution SAR imagery and ice motion are available for detailing the smaller-scale features and polynya dynamics. Section 4 reviews the method used to retrieve ice thickness retrieval from the MODIS IST. The relationship between thin ice thickness and the AMSR-E 36 GHz V/H ratio [*Martin et al.*, 2004, 2005] is reexamined within the context of the Ross Sea polynyas. The AMSR-E derived ice thickness is then used in section 5 as a basis for assessment of the behavior of the NT2 and ABA ice concentration retrievals in largely homogeneous thin ice regions. The last section summarizes the paper.

2. Data Description

### 2.1. Envisat SAR Data, Ice Motion, and Land Mask

[7] Over a 3-month period between mid-April and mid-July of 2005, almost daily Envisat C-band SAR images of the eastern Ross Sea were acquired and downlinked to the McMurdo Reception Facility. The recorded radar data were relayed to White Sands via a communication satellite, shipped by courier to the Alaska Satellite Facility to be processed and finally delivered to the Jet Propulsion Laboratory (JPL) for geophysical analysis. The data were provided as part of a joint project of the National Ice Center (NIC) and JPL, supported by the European Space Agency (ESA) and NASA, to demonstrate the feasibility of a near real-time link for operational use of Envisat acquisitions in the Southern Ocean. Our analysis utilizes this SAR data set. The ice velocities used in this paper are derived by the tracking of common ice features in the SAR imagery [*Kwok et al.*, 1990]. To minimize coastal contamination due to the motion of the ice front, the land mask used in this work is derived from the SAR imagery.

2.2. Other Data Sets

[8] The 1-km MODIS IST swath data, the daily 12.5-km gridded fields of AMSR-E brightness temperature and derived ice concentration data sets are provided by the National Snow and Ice Data Center (NSIDC). The MODIS swath-based fields are resampled onto the polar stereographic projection for coregistration with the gridded AMSR-E and SAR data. Sea level pressure fields are from analysis products of the European Center for Medium-range Weather Forecasts (ECMWF). The ECMWF data set contains the high-resolution output from the ECMWF operational model on a Gaussian (n80) grid with resolution of about 1.125 degrees.

3. Ross Sea Polynyas

[9] This section provides a general description of the Ross Sea polynyas and then a more detailed description of the observed dynamics and variability at the RIS ice front for a 20-day period in June 2005. The results here illustrate at fairly high resolution the spatial and temporal length scales of the polynya events off the ice front.
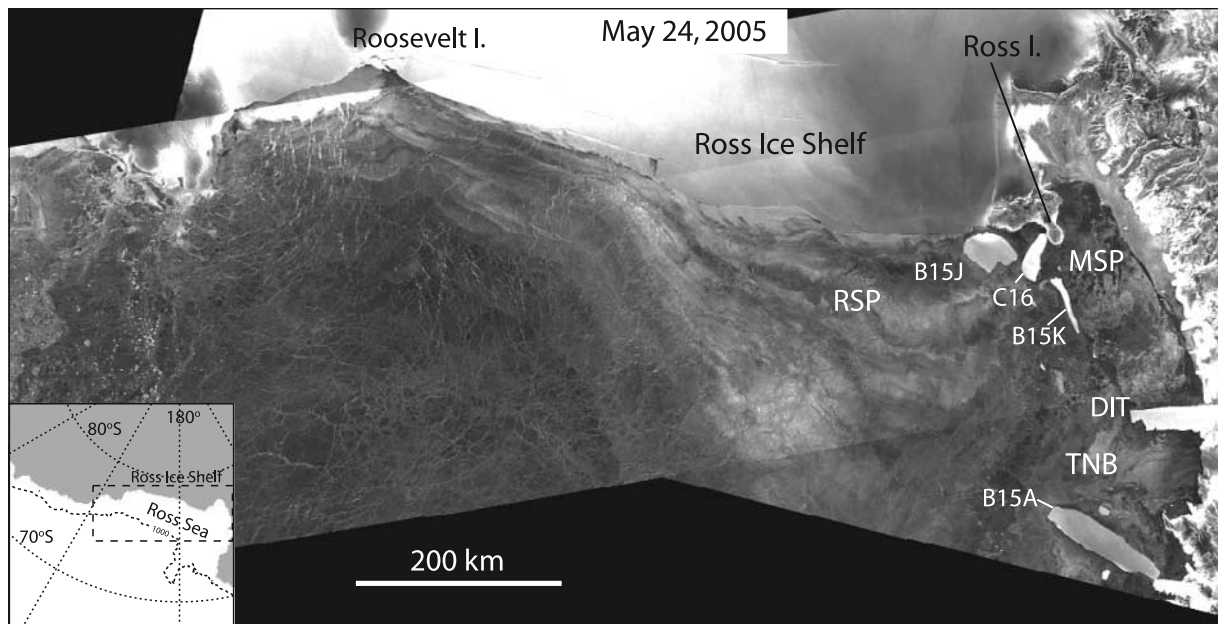
Figure 1. Envisat synthetic aperture radar (SAR) images of the Ross Sea south of ~74°S. This mosaic, constructed from images acquired on 24 May 2005, shows the sea ice cover north of the Ross Ice Shelf. The following polynyas are identified on the image: the Ross Sea polynya (RSP), the Terra Nova Bay polynya (TNB), and the McMurdo Sound polynya (MSP). Also shown are the locations of the Drygalski Ice Tongue (DIT) and Roosevelt Island. Inset shows the location of the 600 km by 1180 km area covered by the SAR image. (Envisat image ©ESA 2006.)

3.1. General Description

[10] An Envisat image mosaic from 24 May 2005 (Figure 1) shows the location of the three largest Ross Sea polynyas; they are the Ross Sea Polynya (RSP), the Terra Nova Bay Polynya (TNB) and the McMurdo Sound Polynya (MSP). These polynyas are important in that their ice production and associated salt rejection contribute to the formation of a dense water mass, the High Salinity Shelf Water (HSSW) that is a source of Antarctic Bottom Water [*Jacobs and Comiso*, 1989; *Jacobs et al.*, 2002]. The RSP includes all the polynya areas created at the RIS front between 160°W and Ross Island. Average winter RSP coverage is not uniform along the ice front but is largest west of 180°W. Geographically, Terra Nova Bay covers an area of ~6000 km² in the western Ross Sea and is bordered on the south by the floating Drygalski Ice Tongue (DIT) and on the north by Cape Washington [*Van Woert*, 1999]. The smaller McMurdo Sound Polynya, between Ross Island and the Scott Coast, remained relatively inactive during the early winter of 2005; the almost immobile thick sea ice cover within the sound is due to blockage of the opening into the Ross Sea by the large grounded icebergs B15J, B15K and C16.

[11] Dominant southerly airflow and associated katabatic winds over the western Ross Ice Shelf are the primary atmospheric forcing for development and variability of the Ross Sea polynyas [*Bromwich et al.*, 1993]. *Bromwich et al.* [1998] find that about 60% of the polynya events are linked to katabatic wind events (from the ice shelf); the remaining 40% are due to katabatic drainage winds (down-slope from outlet glaciers) and barrier winds that flow northward along the Transantarctic Mountains and then deflected eastward by topographic barriers along the Scott Coast.

3.2. Bands in SAR Imagery Associated With Polynya Events

[12] Figure 2a shows the winds for a 20-day period between 5 and 25 June 2005. The sequence of three SAR images, AMSR and motion fields on 14 June, 19 June, and 23 June (Figures 2b, 2d, and 2f) show snapshots of the development of the sea ice cover seaward of the Ross Ice Shelf (RIS). Nearly parallel bands seen in the SAR data are likely associated with the quasiperiodic winds (Figure 2a) measured at an automatic weather station (VITO) at 78.5°S, 177.8°E (installed in February 2004) located closest to the ice front (solid square in Figure 2c). Between 5 and 20 June, the 2-m winds are predominantly off the ice shelf with speeds that ranges up to 20–30 m/s. These winds maintain the polynya and transport the ice cover northward. The ice motion of the seaward edge of the bands (Figures 2c and 2e) is derived from a sequence of near-daily Envisat SAR imagery (Figure 2b). Five bands are clearly visible in the imagery. Band 1, created by a polynya event around 5 June (imagery not shown here), is the oldest and thus contains the thickest ice. Subsequent bands, labeled by their order of creation, consist of younger and thinner ice. Similarly, within each band, the age and thickness of the ice increases seaward from the edge of one band to the next. The bands span a distance of 650 km from end to end and extend nearly the length of the Ross Ice Shelf from the Bay of Whales to Ross Island.

[13] In the SAR imagery (Figures 2b, 2d, and 2f), the polynyas are made visible by the brighter parallel wind-
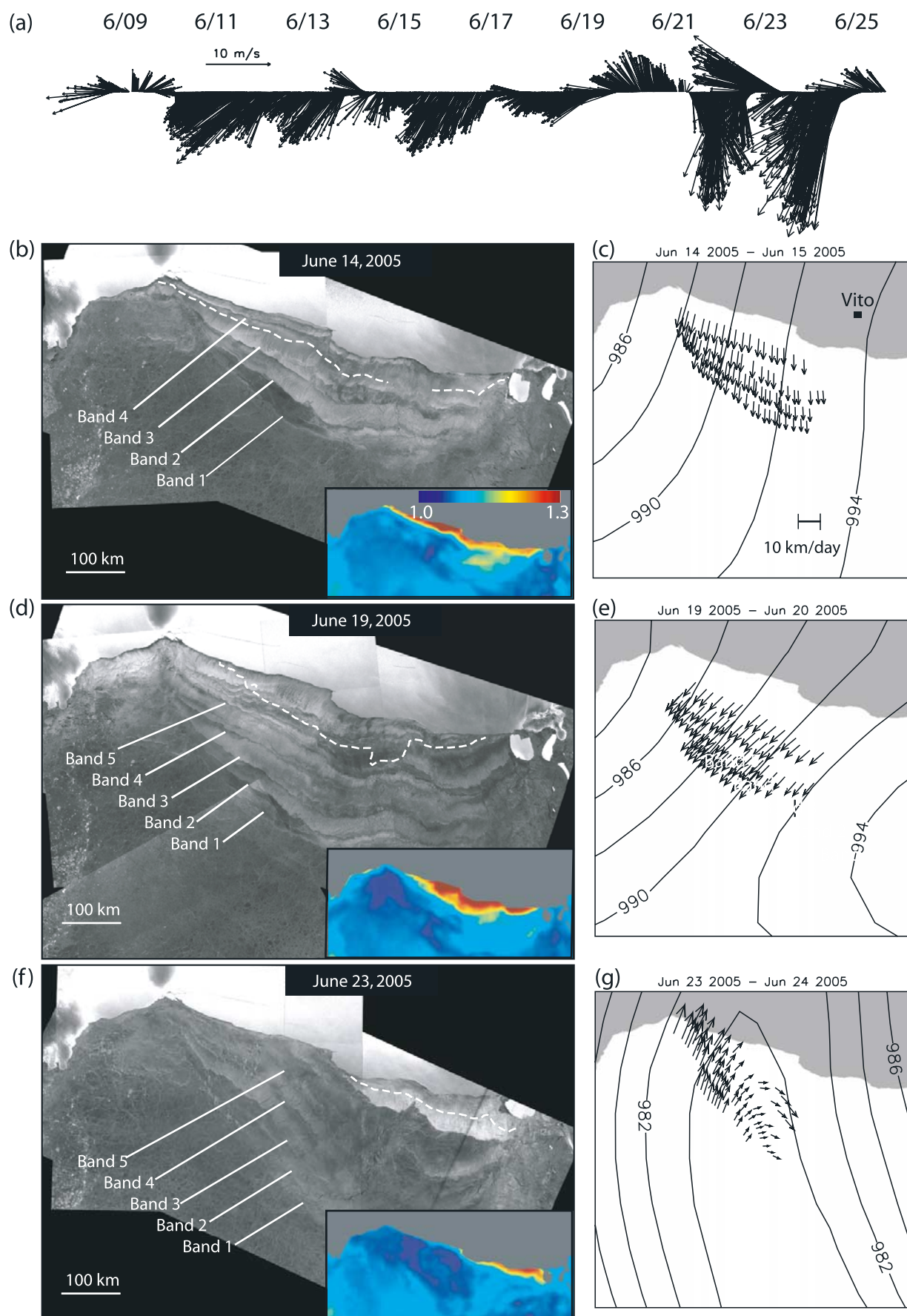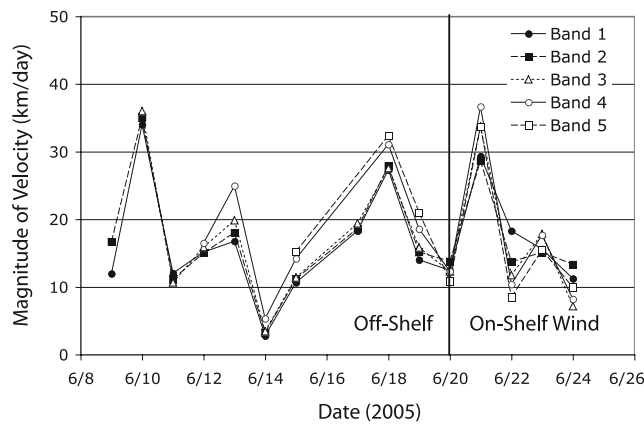
Figure 2

Figure 3. Magnitude of average ice motion at the band fronts. On the eastern Ross Sea, the wind is off-shelf prior to 20 June and on-shelf after that.

generated Langmuir streaks oriented perpendicular to the ice shelf [*Martin*, 1981; *Drucker et al.*, 2003]. The bright and dark radar backscatter features within the polynya region are associated with frazil and pancake ice formation. This is evident in the polynyas just north of the ice front. Downwind of the ice shelf, there is rapid formation of frazil and pancake ice with distance. Features resembling the streaks appear to have been imprinted in the ice and are clearly visible in the radar imagery of the older bands. At this stage of development, the ice in the bands has a different character and appears more homogeneous than the rest of the Ross Sea ice cover, which is characterized by floes of varying sizes and fracture patterns. The widths of the bands decrease slightly as they are advected downwind, suggesting convergence associated with ice deformation. The mechanism responsible for creating the delineations (backscatter contrasts) between the different bands, which are faintly visible as lineaments with lower surface temperature and not visible at all in the AMSR-E images, is not clear. Since radar backscatter is more sensitive to small-scale surface relief, we speculate that the contrast in radar backscatter between bands could be due to rafted ice and perhaps snow filled to the lee of these structures. At this thickness, rafting is more likely. Another possibility is that smoother ice is generated during lower wind conditions.

[14] On 19 June (Figure 2d), the widths of the bands (beginning with Band 1) are approximately 30 km, 32 km, 43 km, 45 km and 80 km. On this date, the edge of Band-1 is ~230 km from the ice front and the ice area created by these polynya events cover ~100×10^3 km^2, almost a quarter of the shelf area between the ice front and the 1-km isobath. This is a significant displacement of the edge of Band-1 which, for the 15-day period, translates into a mean

ice motion of ~15 km/day. Figure 3 shows the actual variability in the daily ice speed, which ranges to over 35 km/day. After 20 June, the winds reverse direction in the eastern Ross Sea and the northerly wind pattern causes the ice to converge. The 23 June image and ice motion (Figure 2f) seem to indicate that, because of the wind field (on-shelf in the east and off-shelf in the west), the openings in the eastern RIS have closed while the polynya in the western Ross Sea remains open. It is interesting to note that the displacements of the younger bands are higher (Figure 3) than the older bands when the winds are off-shelf and the opposite after wind reversal some time after 21 June. This can be attributed to the associated ice deformation and the increase in ice strength associated with convergence on the ice front.

[15] To understand the wind-driven response of the thin polynya ice, we examine the linear relationship between the SAR ice velocity u, the geostrophic wind G, and the mean ocean current c, of the form $u = AG + c + \varepsilon$. A is a complex coefficient where the magnitude $|A|$ is typically referred to as the scaling factor between the speed of the wind and ice, and an angle θ representing the turning of the ice to the left (+) or right (−) of the wind. The symbol ε represents that part of the ice velocity that is neither a constant nor a linear function of the wind. The geostrophic wind $\vec{G}$ (= $-\frac{\vec{k}}{f\rho} \times \nabla P$), where: f is the Coriolis parameter; ρ is the air density; P is the sea level pressure; and $\vec{k}$ is the surface normal, is derived from the ECMWF surface pressure fields. Using motion estimates at the edges of the bands, the regression results show that the ice moves with a speed of ~2.1% and ~13° to the left of the geostrophic wind. The squared correlation between the two quantities is ~0.8. This can be compared to the results of *Kwok* [2005] from the Ross Sea which consider only ice motion more than 300 km from the coast. These results give a scale factor and turning angle of ~1.7% and 4°, with squared correlations that vary between 0.4 and 0.76. The higher scaling factor and turning angle seem consistent with a thinner, newly created ice cover in a near free-drift situation. Because of the small size of our data set, we did not examine the effect of the ocean current, c, or investigate the local variability of A.

4. Thin Ice Thickness From MODIS and AMSR

[16] We use the ice thickness from the nearly homogeneous polynya areas as a basis for examining the behavior of the AMSR-E ice concentration algorithms. In this section, we provide a brief description of the thickness retrieval used in the present work (developed elsewhere). The clear-sky limited MODIS ice thicknesses are used to assess the efficacy of the more generally usable (i.e., not clear-sky limited) AMSR-E ice thickness algorithm (described by *Martin et al.* [2004, 2005]) in the Ross Sea, an approach

Figure 2. Sea ice bands in the Ross Sea Polynya (RSP) associated with quasiperiodic off-shelf winds. (a) Wind velocity measured at the automatic weather station VITO; the solid square in Figure 2c shows its location (78.5°S, 177.8°E) on the Ross Ice Shelf. The coordinate system of the wind vectors is aligned with the axes of the image. (b, d, f) SAR images of the developing bands; insets show the corresponding AMSR-E R_{36} fields. Dashed line shows the 10-cm thickness isopleth derived from AMSR. (c, e, g) Ice motion at the seaward edge of these bands. The image sequence is from 14 June, 19 June, and 23 June. (Band 1 contains the oldest (chronological) ice and Band 5 the youngest. Isobars are from ECMWF sea level pressure fields (contour intervals: 2 hPa). (Envisat image ©ESA 2006.)
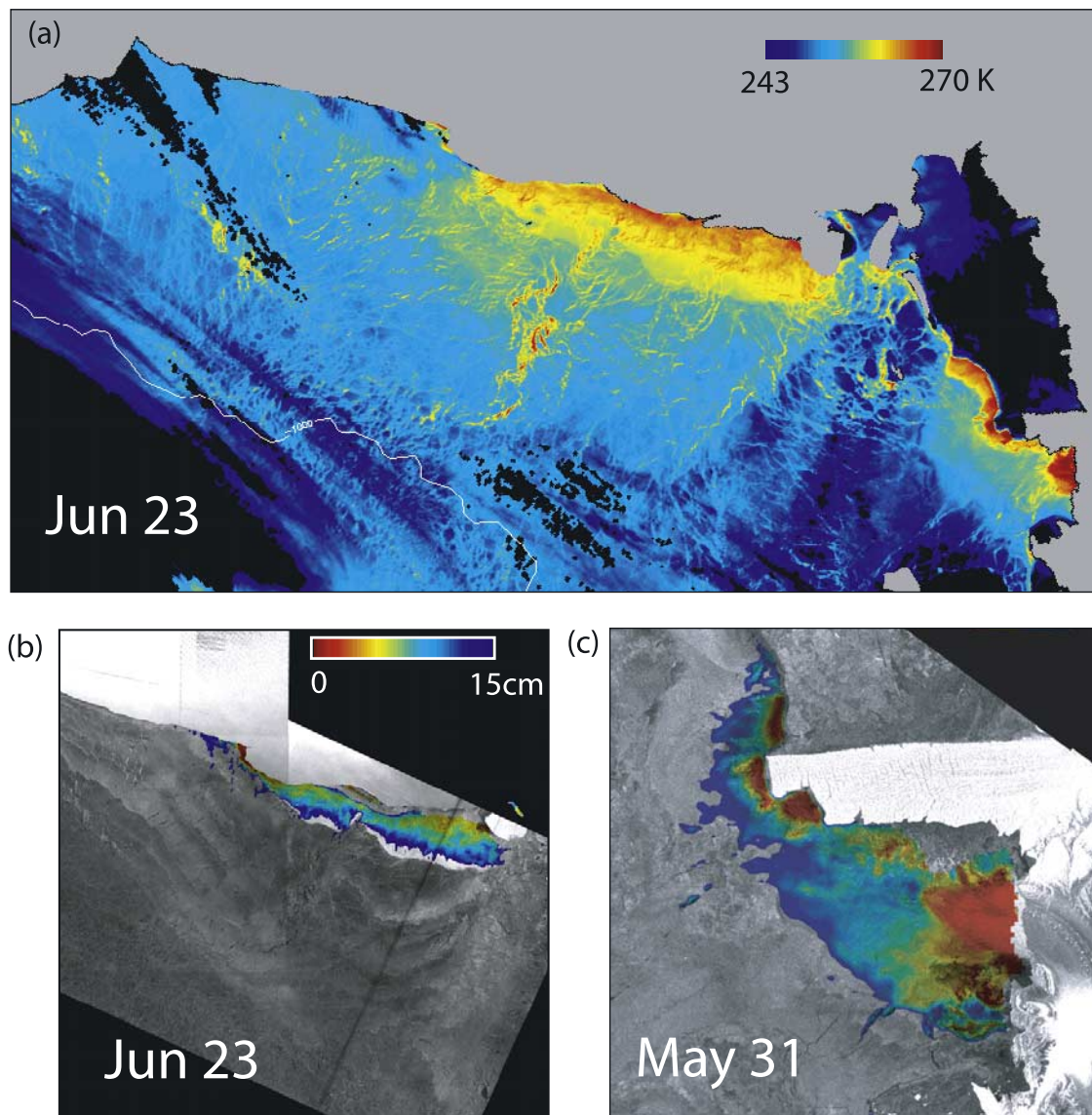
Figure 4. Three examples of ice surface temperature fields and thin ice thickness (0–15 cm) derived from MODIS fields. Note that the Terra Nova Bay example is not from 23 June because there was no SAR coverage on that date. (a) Ice surface temperature of the Ross Sea region (23 June). This image is not entirely cloud-free everywhere; it is chosen to show a broad view of the Ross Sea including both the Ross Sea and Terra Nova Bay Polynyas. (b, c) MODIS-derived ice thickness at the Ross Sea (23 June) and Terra Nova Bay (31 May) Polynyas overlaid on near coincident SAR images. The MODIS IST is at 1-km resolution; the SAR data resolution is degraded to match that of MODIS. (Envisat image ©ESA 2006.)

that has been successfully applied to the analysis of the Chukchi Sea polynya.

4.1. Ice Thickness From MODIS

[17] The basis of the MODIS approach (described by *Yu and Rothrock* [1996] and *Drucker et al.* [2003]) is that the surface temperature of sea ice decreases with thickness. Physically, the surface temperature of bare thin ice (<15–20 cm) is closer to the freezing point of water at the bottom boundary, while the surface temperature of thick ice is closer to that of the air temperature. On cloud-free days during winter, this large thermal contrast between thick and thin ice can be effectively used to retrieve ice thickness

using IST estimates from the thermal infrared channels of MODIS. An IST map of the Ross Sea region (Figure 4a) derived from MODIS radiances at 11.0 μm and 12.0 μm (channels 31 and 32) shows the contrast between the warmer polynyas and the surrounding ice cover. The IST field on a 1 km by 1 km grid is a standard MODIS product (available at the National Snow and Ice Data Center (NSIDC)). *Hall et al.* [2004] give the details of its derivation and expected uncertainties; they report that when visual cloud screening is performed to eliminate MODIS pixels thought to be contaminated by fog, results improved; their best estimate of the IST uncertainties is 1.3 K.

(a) Jun 23 (RSP)

(b) Jun 14 (TNB)
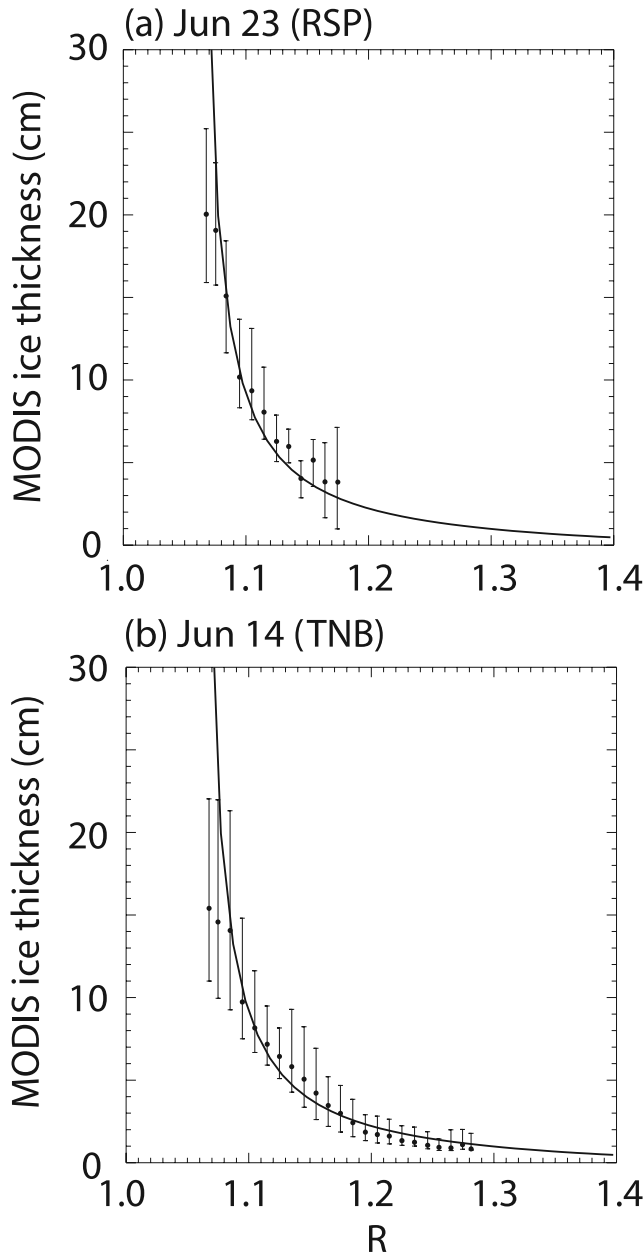
Figure 5. Plot of MODIS-derived ice thickness on the vertical axis and AMSR-E 36 GHz V/H brightness temperature ratio on the horizontal axis. (a) Ross Sea Polynya. (b) Terra Nova Bay Polynya. The solid curve shows the ice thickness versus 37 GHz SSM/I V/H relationship described by *Martin et al.* [2004]. See text for further description. Comparisons are only for samples within 100 km of the ice front.

[18] Ice thickness is retrieved according to the algorithm of *Drucker et al.* [2003]. Briefly, in the surface heat balance, they assume the following: the ice is thin (<20 cm), the water temperature is constant at $-1.8°C$, and the temperature profile is linear within the ice. Setting the heat flux through the ice equal to the atmospheric flux then allows us to solve for ice thickness. In these calculations, the 2-m wind and air temperature are from ECMWF. Uncertainties in the retrieval increase with thickness because of decreas-

ing contrast with surrounding ice; *Drucker et al.* [2003] discuss the sources of error. For the retrieval to work, the required surface conditions are that the air-ice interface is below freezing and snow-free. Perhaps the more difficult requirement of this algorithm is that of clear-sky conditions because clouds and water vapor can easily contaminate IST retrievals. Since the MODIS cloud masks used in producing the IST fields may not effectively remove all contaminated samples; residual clouds and fog are sources of error. In our study, we select only the very clear days by visually screening the MODIS IST fields; only images containing cloud-free regions with sharply defined features are used.

[19] Figures 4b and 4c show two examples of MODIS-derived thin ice thickness maps of the RSP (on 23 June) and TNB (on 31 May) polynyas overlaid on near-coincident SAR images. At the RSP, thin ice is seen only in the youngest bands closest to the ice shelf. The gradation of color (red to blue) with distance shows the expected thickening due to rapid ice growth downwind from the RIS. In this particular image, the ~10-cm-thick ice is at a distance of 20–25 km from the ice front. At an average motion of ~10–15 km/day between 22 June and 23 June, this thickness represents 1–2 days of growth. The 10-cm isopleth in the TNB polynya example extends ~20–25 km into the Ross Sea; also visible are smaller polynyas formed at the tip of the Drygalski ice tongue.

4.2. Ice Thickness From AMSR

[20] Previous work by *Steffen and Maslanik* [1988] and *Wensnahan et al.* [1993] have suggested the possible use of polarization differences for detection of thin ice. Recently, *Martin et al.* [2004] showed that the thickness of thin ice could indeed be derived from an algorithm based on the ratio of the SSM/I 37-GHz 25-km resolution vertical and horizontal brightness temperatures. For thicknesses less than 10 cm, the retrieval results compare well with thicknesses derived from clear-sky AVHRR data. Further, *Martin et al.* [2005] adapt this SSM/I 37-GHz ice thickness algorithm to the AMSR-E 36-GHz channels, and show improvements in ice thickness/heat flux estimates over the Alaskan coast Chukchi Sea polynyas; higher spatial resolution allows for the accounting of heat flux from smaller polynyas.

[21] This passive microwave SSM/I thin ice algorithm depends on the change in the surface salinity with ice thickness that occurs for thin ice, and uses the ratio of the 37V and 37H gridded brightness temperatures. The thin ice thickness, h, as a function of the brightness temperature ratio, $R_{37} = T_{B37V}/T_{B37H}$, has the following exponential form [*Martin et al.*, 2004]:

$$h = \exp[1/(\alpha R_{37} + \beta)] - \gamma, \tag{1}$$

where $\alpha = 230.5$, $\beta = -234.6$ and $\gamma = 1.008$. The constants in this relationship are derived by comparison of the ratio (R_{37}) with AVHRR ice thickness (h). As Figure 5 shows, equation (1) describes a monotonically decreasing curve that is steep for R_{37} close to unity. When $R_{37} < 1.1$, the ratio is not sensitive to changes in ice thickness. It can be seen that the curve is best for retrieval of ice thickness for the range between 0.5 to 10 cm, or R_{37} between ~1.4 and ~1.1. In terms of uncertainty, between 0.5 and 5 cm the
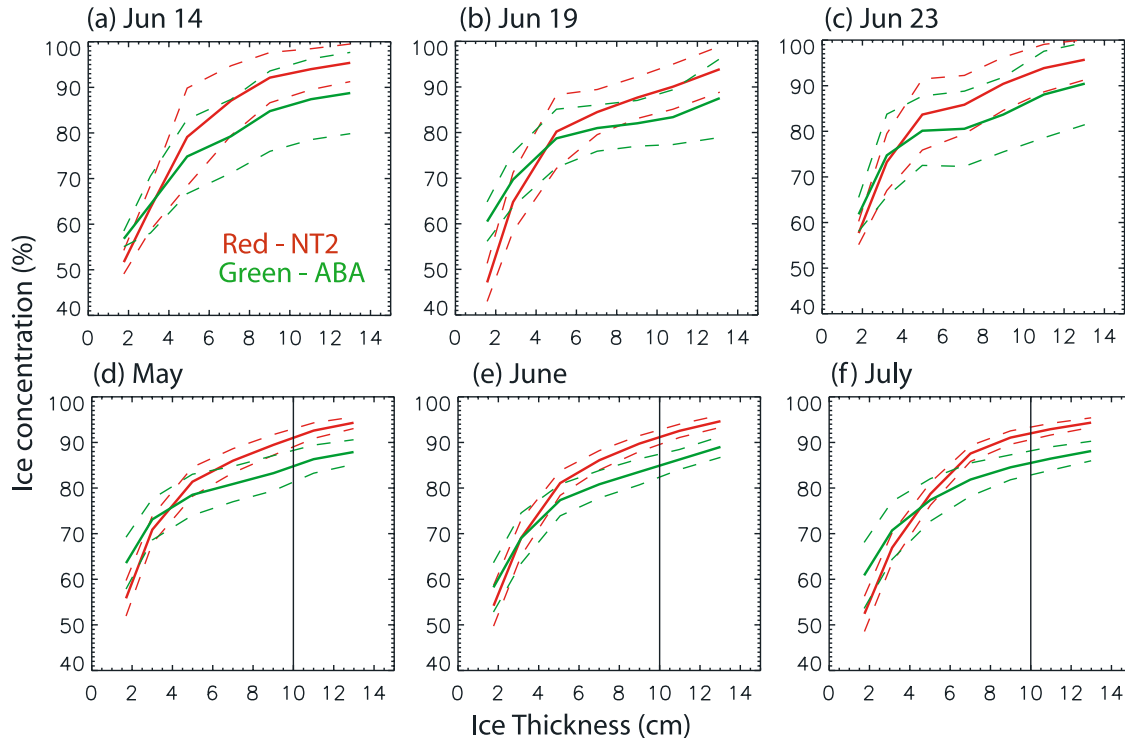
Figure 6. Relationship between AMSR-E ice concentration (from NT2 and BBA) and AMSR-derived thin ice thickness within 100 km of the ice front: (a) 14 June, (b) 19 June, (c) 23 June, (d) May, (e) June, and (f) July. Figures 6d, 6e, and 6f are monthly means. The mean values (solid line) and standard deviations (dashed line) are computed within 2 cm intervals; the x values of each point represent the average thickness within the intervals.

thicknesses have a standard deviation of about 1 cm; for thicknesses as large as 12 cm, the standard deviation is about 2 cm. To adapt the relationship in equation (1) for use with the AMSR-E 36 GHz data, we follow the procedure of *Martin et al.* [2005]. The relationship between R_{37} and R_{36} is first obtained by daily linear regression of the two variables over the ice-covered part of the Ross Sea. The regression coefficients are then used to adjust the R_{36} values. This cross-calibrates the two data sets and additionally corrects for the seasonal drift of the AMSR-E data relative to the SSM/I data. For compatibility of spatial resolutions, the AMSR-E pixels are degraded to that of SSM/I pixels (25-km) before comparisons. Procedurally, we derive ice thickness from the AMSR-E R_{36}-ratio by first mapping it to R_{37} and then equation (1) is used to compute h. Caveats on surface conditions for application of this algorithm are similar to that of the MODIS algorithm; that is, the air-ice interface is not melting and the ice is free of snow. Also, any changes in surface salinity due to flooding will alter the thin ice signature and will be a source of error in the analysis.

[22] The insets in Figures 2b, 2d, and 2f show the AMSR-E 36 GHz V/H (R_{36}) fields for corresponding to the SAR image sequence. Also shown are the 10 cm isopleths derived using the above procedure. The fields show that thin ice (<10 cm), associated with the larger R_{36}-ratio, is located adjacent to the ice front and within the youngest bands of the polynya. The features in the AMSR-E fields can be compared to the features in the SAR image but the

banding, as noted earlier, is not evident in the AMSR-E data. The shift in the polynya locations in the eastern RIS during 14 and 19 June to its location in the western RIS on 23 June is clearly captured.

[23] We also note that ice parallel to the edge of the SAR bands should represent ice of approximately the same age. Assuming nearly uniform wind and surface temperature history, it is expected that thickness isopleths should also be nearly parallel to the bands. Figure 2b shows that other than a few mismatches, this is true. Given the general coherence of the contours and the isopleths, the following section examines the robustness of the thickness algorithm through comparative analysis with derived MODIS ice thicknesses.

4.3. Relationship Between MODIS Ice Thicknesses and AMSR-E R_{36}

[24] To assess the effectiveness of equation (1) in the retrieval of thin ice thickness in the Ross Sea, we plot the MODIS derived ice thickness, h_M, against the ratio of the vertical and horizontal brightness temperatures (R_{36}). As described above, R_{36} is first cross-calibrated with R_{37}. The comparisons at the RSP (Figure 5a) and TNB (Figure 5b) for two cloud-free days are plotted separately to see whether there are regional differences in the results that could be due to variability in ice production processes. To reduce the effect of snow accumulation on older ice, we compare only those young ice areas within 100 km of the ice front. These ice areas contain the youngest sea ice formed in the polynyas and thus the
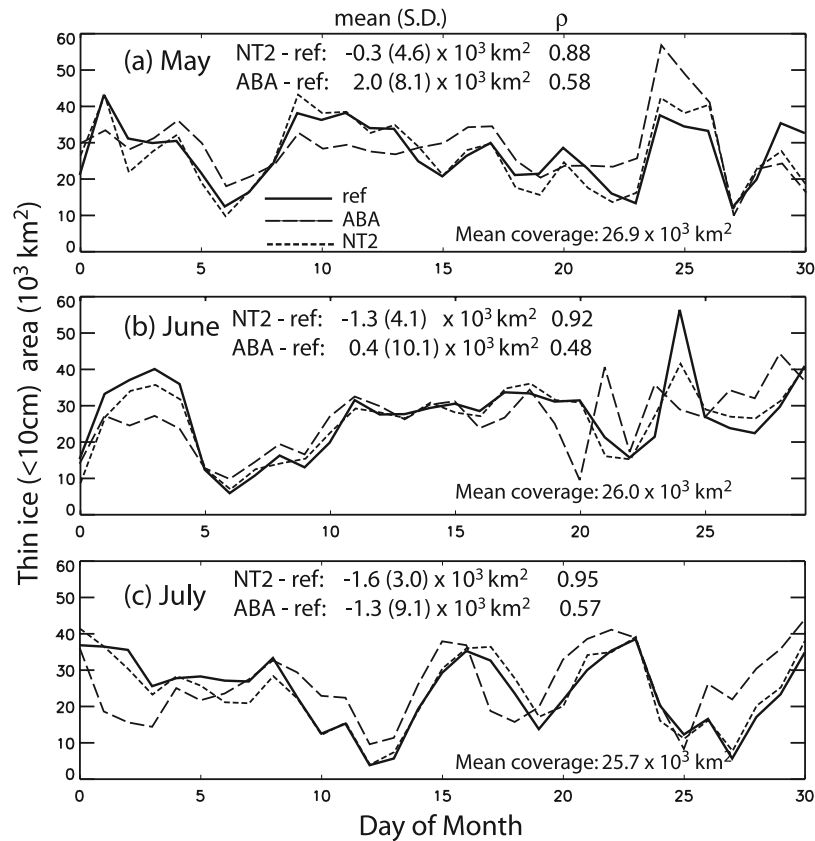
Figure 7. Daily polynya areas of the Ross Sea within 100 km of the coast/ice front from AMSR-E ice thickness and NT2 and ABA ice concentration fields: (a) May, (b) June, and (c) July. Differences (mean and standard deviation) and correlation coefficients between the time series from NT2/ABA and the 10-cm contour (ref) are shown for each month. The monthly mean coverage is also shown.

likelihood of immediate snow accumulation on these surfaces should be lower.

[25] The relationship between h_M and R_{36} (Figure 5) compares well with the empirically derived behavior described by equation (1). The mean values and standard deviations of the retrieved thickness in Figure 5 are computed within intervals of 0.01. The mean values (solid dots) are generally within a centimeter or two of the predicted thickness. Only a narrow range R_{36} are sampled in the RSP polynya (Figure 5a); the TNB results (Figure 5b) represent a larger range of R_{36} (up to ∼1.3). For the open ocean, the value of R_{36} approaches 1.6 but there are no values that approach this limit in the examples because of the mixture of thin ice and open water within an AMSR-E pixel. The uncertainties are lower for thinner ice and higher for thicker ice. For $R_{36} < 1.1$, the uncertainties are ±5 cm.

[26] One source of variability in comparison of the MODIS ice thickness and R_{36} is that the two data sets are not coincident in time. The AMSR-E brightness temperature fields represent daily composites while the MODIS fields are taken at a point in time. Therefore, there is some smearing of the R_{36} fields due to the ice growth and ice motion. An average ice motion of ∼20 km/day (Figure 3) represents the smearing of the surface over 1–2 AMSR-E resolution elements in the daily composites. For a steady off-shelf wind, the smearing is less of an issue when newly formed ice is advected downwind and the gradient in ice age with distance from ice front is maintained; that is, the AMSR-E pixels sample approximately the same ice thickness field. The worst case is when the wind changes direction (say, from on-shelf to off-shelf) between AMSR-E passes, then the microwave signatures of sea ice with different thicknesses (centimeters) would be mixed. The retrieved thickness would not be an average value; it would be thicker because of the nonlinearity of equation (1). Another source of error is the residual atmospheric effects of high clouds and warm fog on the IST data. Discussed in the work of *Martin et al.* [2004], these have confounding effects on the MODIS retrievals depending on whether they occur over the polynya or the adjacent ice pack. For this work, only the clearest days are used. As for contamination of the sea ice pixels by land, we use land masks that are derived from high-resolution Envisat SAR imagery to minimize this effect.

[27] The relationship in equation (1) seems fairly robust. Using an identical method to *Martin et al.* [2004], which compares SSM/I- and AVHRR-derived thin ice thickness, we show that: (1) nearly the same relationship is obtained by performing a similar analysis with AMSR-E and MODIS data; and, (2) it seems applicable to the Ross Sea polynyas examined here. This provides confidence for its general use when the restrictions discussed above are heeded. Even though the numbers of different processes that can modify the ice structure appear to be large, satellite imagery
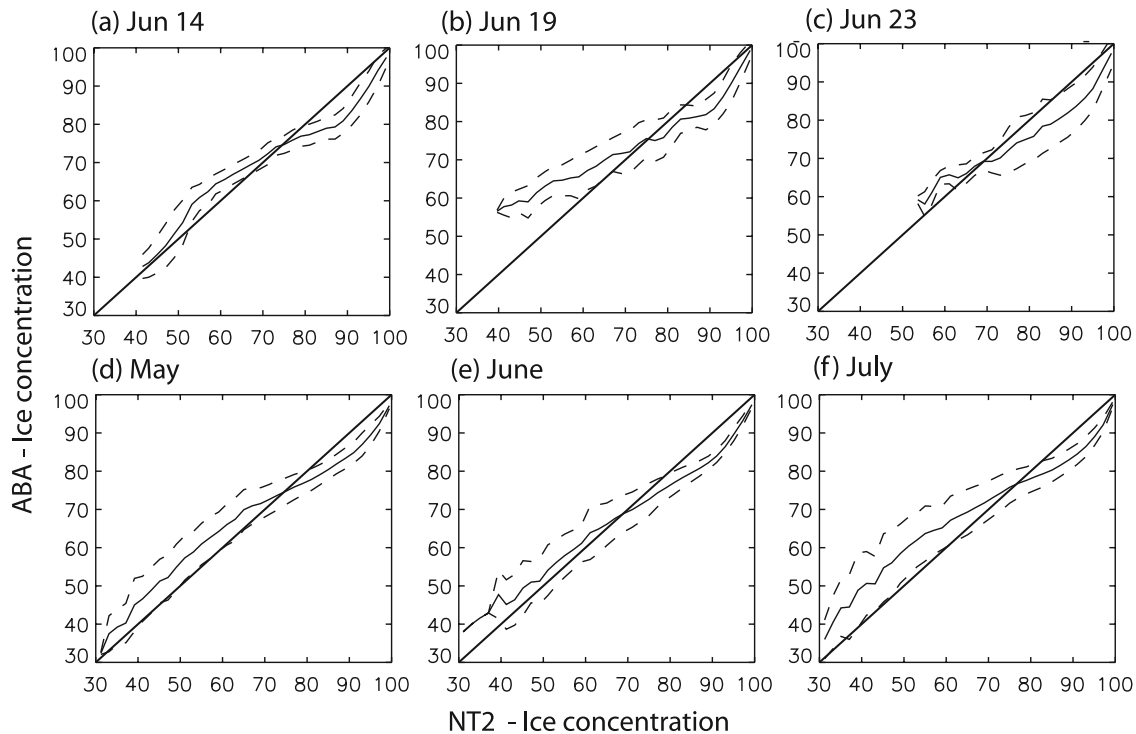
Figure 8. Relationship between NT2 and ABA ice concentration estimates within 100 km of the Ross Sea coast and ice front: (a) 14 June, (b) 19 June, (c) 23 June, (d) May, (e) June, and (f) May. The solid and dashed lines connect the mean values and standard deviations computed within 2% ice concentration intervals.

suggests that the microwave signatures develop in relatively reproducible orderly sequences, and that obtaining estimates of thin ice thickness is practical. Thus, although the relative importance of the various physical processes is not entirely understood [*Wensnahan et al.*, 1993], these processes appear to occur in regular progression and give relative statistical homogeneity over large areas.

## 5. Assessment of Ice Concentration Retrievals

[28] The relationship in equation (1) allows the derivation of the thickness of thin ice in polynyas directly from AMSR-E data. Even though atmospheric effects are not entirely absent in the passive microwave data, we are no longer restricted to cloud-free days. Here we use the derived ice thickness as the basis for examining the response of the NT2 and ABA algorithms to a near-homogeneous field of thin ice. The present assessment does not address the response of these algorithms to a mixture of first-year ice and water near the ice edge.

5.1. Relationship Between Ice Concentration and Thickness

[29] Figure 6 shows the mean and variability of the dependence of the NT2 and ABA ice concentrations on the AMSR-E derived ice thickness within 100 km of the coast. For 2-cm bins, the solid and dashed lines connect the mean values and standard deviations. Here we examine the daily behavior of this relationship for three days in June (14, 19, and 23) corresponding to the 3 days shown in Figure 2, and

examine the average monthly behavior for May, June and July.

[30] From both the NT2 and ABA approaches, the effect of large areas of thin ice in lowering the ice concentration estimates is clear. This can be attributed to the fact that thin ice signatures lie between those of open water and first-year ice. Qualitatively, the response is characterized by a steep rise in the apparent ice concentration during the first several centimeters of ice growth followed by a more gradual increase. Above 4 cm, and because of the steeper initial response of the NT2, the mean NT2 ice concentrations are generally higher than the ABA estimates. The response to increases in ice thickness slows above 6−8 cm. Beyond this thickness, the NT2 estimates are consistently higher by ∼10%. As seen in the daily samples and the monthly averages, the results show that even though the two algorithms respond differently to thin ice, they do so consistently and reproducibly. Compared to the monthly results, the daily responses are noisier. Figure 6 shows that the variability in response is high, 5% in the daily fields and a somewhat lower 2% in the monthly fields. Some of the variability could be attributed to the uncertainties inherent in the thickness and ice concentration retrievals used in the present analysis. In addition, the procedures respond nonlinearly to changes in the microwave signatures of thin ice. On the whole, these results define the approximate spatial correspondence between ice thickness and ice concentration isopleths. From the monthly analyses (Figures 6d, 6e, and 6f), an ice thickness of 10 cm corresponds to ∼83 ± 3% and ∼91 ± 2% ice concentration in the ABA and NT2 estimates.
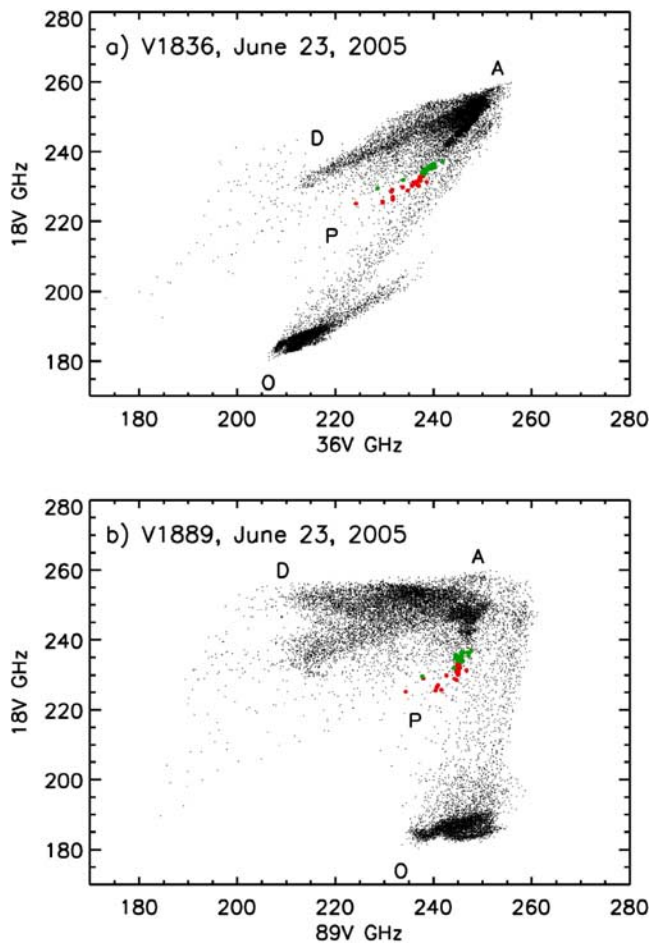
Figure 9. Scatterplot of the brightness temperatures from the 18, 37, and 89 GHz channels in the Ross Sea on 23 June: (a) 18 GHz versus 36 GHz (V1836) and (b) 18 GHz versus 89 GHz (V1889). Thin ice samples adjacent to the ice shelf are shown in red while the ones 100 km away are shown as green. A and D represent data in the consolidated ice regions while the data points at O represent those in open water regions.

[31] Indeed, an immediate application of the results obtained in this section is in computing the polynya coverage by defining its perimeter as the 10-cm thickness contour. This follows from the point noted by *Martin et al.* [2004] that the area covered by sea ice less than 10 cm thick captures about 90% of the polynya heat loss. Since the 83% (ABA) and 91% (NT2) isopleths correspond to approximately the 10-cm thickness contour (Figures 6c, 6d, and 6e), we examine the consistency of the estimated daily polynya coverage by comparing their areas within the defined isopleths (i.e., <83% for ABA, and <91% for NT2) with that computed directly from the AMSR-E-thickness fields. Figure 7 shows the daily coverage results for May, June and July. First, the average coverage of ∼26,000 km² (with the MSP contribution) is comparable to that obtained by *Martin et al.* [2007]. Second, the mean and variability of the NT2- and ABA-derived polynya areas are correlated and consistent with the areas derived directly from the AMSR-E thickness estimates (see values in Figure 7). The correlation coefficients, mean differences,

and standard deviation of differences do not vary significantly from month to month. The 3% (ABA) and 2% (NT2) variability in the isopleths (Figures 6d, 6e, and 6f) translate into uncertainties in polynya coverage of 2700 km² and 1800 km². Third, this suggests that the relationships shown in Figure 6 could be useful for estimating polynya coverage with either the ABA or NT2 analyses. These comparisons also show that the NT2 coverage estimates are in better agreement (higher correlation and lower variability) with the coverage from AMSR-E thickness estimates. We suspect that the better correlation between the NT2 ice concentration and derived thickness could be due in part to the near linear relationship of R (in the range between 1 and 1.5) with the polarization ratio $PR = \frac{(R-1)}{(R+1)}$) used by the NT2 algorithm. Further understanding of these results is important since they suggest that the same relationship might be used to estimate ice thickness within the polynya.

5.2. Relationship Between the NT2 and ABA Analyses

[32] It is also instructive to compare coincident NT2 and ABA results to identify any systematic differences between the two data sets. For the region within 100 km of the coast, Figure 8 shows the relationship of the ice concentration analysis from the two approaches for the same three days and three months used in the previous analyses. The abscissa and ordinate axes range from 30% to 100% because there are few samples with less than 30% concentration. The mean values and standard deviations are computed for 2% intervals in ice concentration.

[33] The daily and monthly results show that, above ∼70–80%, the NT2 yields consistently higher concentration estimates than the ABA; differences between the two diverge above 70% then converge above 90%. The largest difference occurs around 90% where the NT2 estimates are higher by ∼10%. This is consistent with the above analysis in that, as Figure 6 shows, the ABA tends to report lower concentrations in the presence of thin ice. Even though there is a concentration-dependent bias between the two schemes, the results show that within bounds their relative behavior are not only consistent but predictable, and characterized by the dependence shown in Figure 8. Below ∼70%, the ABA generally overestimates the concentration relative to the NT2; but since there are few samples of low concentration their relationship is not as well-defined. These differences are expressions of the nonlinear response of each algorithm to the microwave signatures of large areas of thin ice when they are the dominant ice type within the AMSR-E footprints.

[34] To gain insight into the difference in the derived ice concentrations in the thin ice regions, we show scatterplots of the data points in the Ross Sea region on 23 June for 18 GHz (V) versus 37 GHz (V) and 18 GHz (V) versus 89 GHz (V) (Figures 9a and 9b). A key difference in the two algorithms is the utilization of 89 GHz data in the NT2 but not in the ABA. In the plots, the cluster of points between the labels A and D represents data in the consolidated ice regions while the data points at O represent those in open water regions. Data points between O and AD are generally regarded as representing data with different ice concentrations. We isolate the thin ice data points (see Figure 4a) by showing those adjacent to the shelf region in red while the thicker ice farther away is in green. The scales of the

ordinate and abscissa are common to both plots so that the separation of the data points can be seen. Along the abscissa (36 GHz TB for Figure 9a and 89 GHz TB for Figure 9b), a significant difference in separation is apparent between the two sets of data points (red and green); those from the 36 GHz channel show larger separation than those from the 89 GHz channel. In fact, most of the two sets of data points have the same values at 89 GHz. This is, in part, associated with the greater penetration depth at 36 GHz (wavelength of 8.2 mm) so that this channel is more sensitive to thickness than 89 GHz (wavelength of 3.4 mm). As the ice gets thicker, the 89 GHz brightness temperature channel shows very little discrimination [Grenfell et al., 1992] compared to the 36 and 19 GHz channels. As thickness increases, the earlier saturation of the NT2 compared with the ABA, causes the retrieval of higher concentrations for the NT2. The difference at the thinner end in Figure 8 is in part associated with the location of the water tiepoint (i.e., near O in Figure 9) in the two algorithms.

6. Conclusions

[35] The NT2 and ABA algorithms are the two operational algorithms employed by NASA to produce global sea ice concentration estimates from AMSR-E observations. These algorithms do not take into account the transient signature of thin ice, thus large errors can be expected for regions where substantial amounts of such ice are present. For the 3-month in May, June and July 2005, corresponding to a period with available SAR coverage, this note examines the response of the algorithms to extensive areas of thin ice in the Ross Sea polynyas. The thin ice estimates derived from an algorithm using the ratio of the 36-GHz 12.5-km resolution vertical and horizontal brightness temperatures [Martin et al., 2004, 2005] serve as the basis of our assessment. In particular, for the several weeks when SAR data are available, we examine with higher spatial resolution the smaller-scale features and wind-forced advection of the Ross Sea Polynya.

[36] The effect of large areas of thin ice in lowering the ice concentration estimates from both the NT2 and ABA approaches is clearly demonstrated. In general, thin ice has an emissivity that lies between the values for open water and those of first-year ice; thus it has a significant effect on the retrieval if it covers a significant fraction of the footprint. The results show relatively robust relationships between NT2/ABA retrieved ice concentration, C, and thin ice thickness estimates, h (i.e., $C = f(h)$), at the Ross Sea Polynya (RSP) and the Terra Nova Bay Polynya (TNB) (Figure 6). While the two algorithms respond differently to thin ice, the results show that within bounds, they do so consistently and reproducibly as seen in the daily estimates and the monthly averages. These relations define the approximate spatial coincidence between ice thickness and ice concentration isopleths. An ice thickness of 10 cm corresponds to the 83% and 91% ice concentration estimates from the ABA and NT2. For polynyas, this suggests that the retrieved ice concentrations can be used as a proxy for thin ice thickness.

[37] Since the area covered by sea ice within the 10-cm thickness contour contains 90% of the polynya heat loss [Martin et al., 2004], an immediate application of our results is in the calculation of the polynya coverage. Using the ice concentration proxy to define the 10-cm thickness contour, we demonstrate that the daily polynya areas computed using the 83% (ABA) and 91% (NT2) ice concentration isopleths compare well, with quantifiable uncertainties, with those derived directly from the thickness fields.

[38] Both algorithms are affected by thin ice. In this limited domain, the NT2 seems to be less affected thus producing a more accurate estimate, i.e., more ice coverage, according to the strict definitions of ice concentration. Comiso and Steffen [2001], however, point out that ice concentration maps that follow this strict definition would have very limited value since such maps would show practically 100% ice coverage within the ice pack. In the case where use of the ice concentration fields for detection of polynyas or areas of thin ice is of interest, ABA would seem to be more useful because of its more pronounced response at the thin end. Recent work by Comiso et al. [2003] in fact suggest that the relatively lower ice concentration from the ABA (compared to NT2) in coastal Antarctica are likely due to the prevalence of new or young ice in the region, especially coastal polynyas. Furthermore, they suggest that the relative contrast in ice concentration estimates from the NT2 and ABA may be useful in the identification of divergence and polynya regions and perhaps in the quantification of heat and salinity fluxes. However, to use these fields effectively, one has to exercise care in the interpretation of the results and quantify the differential response of the two algorithms. In any case, for an operational product that caters to the general user, the strict definitions of ice concentration must apply.

[39] Even though the areas of thin ice that occur primarily in polynyas occupy a small fraction of the area covered by Arctic and Antarctic sea ice, polynyas are important because they represent locations of significant ice growth combined with intense heat flux and brine production. Especially in the Ross and Weddell Seas, the salt rejection in polynyas contributes to the formation of a dense water mass, the High Salinity Shelf Water (HSSW) that is crucial to the formation of Antarctic Bottom Water. The NT2 and ABA algorithms do not perform optimally in all regions because of the global nature of their approaches. The responses characterized here suggest that, in areas where there are large areas of thin ice, these retrieval procedures could be enhanced to provide additional information about ice thickness.

References

Bromwich, D. H., J. F. Carrasco, Z. Liu, and R.-Y. Tseng (1993), Hemispheric atmospheric variations and oceanographic impacts associated with katabatic surges across the Ross Ice Shelf, Antarctica, *J. Geophys. Res.*, *98*(D7), 13,045–13,062.

Bromwich, D., Z. Liu, A. N. Rogers, and M. L. Van Woert (1998), Winter atmospheric forcing of the Ross Sea Polynya, in *Ocean, Ice, and Atmosphere: Interactions at the Antarctic Continental Margins, Antarct. Res. Ser.*, vol. 75, edited by S. S. Jacobs and R. F. Weiss, pp. 101–133, AGU, Washington, D. C.

Comiso, J. C. (2002), A rapidly declining perennial sea ice cover in the Arctic, *Geophys. Res. Lett.*, *29*(20), 1956, doi:10.1029/2002GL015650.

Comiso, J. C., and K. Steffen (2001), Studies of Antarctic sea ice concentrations from satellite data and their applications, *J. Geophys. Res.*, *106*(C12), 31,361–31,385.

Comiso, J. C., D. J. Cavalieri, and T. Markus (2003), Sea ice concentration, ice temperature, and snow depth using AMSR-E data, *IEEE Trans. Geosci. Remote Sens.*, *41*(2), 243–252.

Drucker, R. D., S. Martin, and R. Moritz (2003), Observations of ice thickness and frazil ice in the St. Lawrence Island polynya from satellite imagery, upward looking sonar, and salinity/temperature moorings, *J. Geophys. Res.*, *108*(C5), 3149, doi:10.1029/2001JC001213.

Grenfell, T. C., D. J. Cavalieri, J. C. Comiso, M. R. Drinkwater, R. G. Onstott, I. Rubenstein, K. Steffen, and D. P. Winebrenner (1992), Considerations for microwave remote sensing of thin ice, in *Microwave Remote Sensing of Sea Ice, Geophys. Monogr. Ser.*, vol. 68, edited by F. F. Carsey, pp. 291–301, AGU, Washington, D. C.

Hall, D. K., J. R. Key, K. A. Casey, G. A. Riggs, and J. J. Cavalieri (2004), Sea ice surface temperature product from MODIS, *IEEE Trans. Geosci. Remote Sens.*, *42*(5), 1076–1087.

Jacobs, S. S., and J. C. Comiso (1989), Sea ice and oceanic processes on the Ross Sea continental shelf, *J. Geophys. Res.*, *94*(C12), 18,195–18,211.

Jacobs, S. S., C. F. Giulivi, and P. A. Mele (2002), Freshening of the Ross Sea during the late 20th century, *Science*, *297*, 386–389.

Kwok, R. (2005), Ross Sea ice motion, flux, and deformation, *J. Clim.*, *18*, 3759–3776.

Kwok, R., J. C. Curlander, R. McConnell, and S. Pang (1990), An ice motion tracking system at the Alaska SAR facility, *IEEE J. Oceanic Eng.*, *15*(1), 44–54.

Markus, T., and D. J. Cavalieri (2000), An enhancement of the NASA Team sea ice algorithm, *IEEE Trans. Geosci. Remote Sens.*, *38*(3), 1387–1398.

Martin, S. (1981), Frazil ice in rivers and oceans, *Annu. Rev. Fluid Mech.*, *13*, 379–397.

Martin, S., R. Drucker, R. Kwok, and B. Holt (2004), Estimation of the thin ice thickness and heat flux from SSM/I data for the Chukchi Sea Alaskan coast polynya for 1990–2001, *J. Geophys. Res.*, *109*, C10012, doi:10.1029/2004JC002428.

Martin, S., R. Drucker, R. Kwok, and B. Holt (2005), Improvements in the estimates of ice thickness and production in the Chukchi Sea polynyas derived from AMSR-E, *Geophys. Res. Lett.*, *32*, L05505, doi:10.1029/2004GL022013.

Martin, S., R. Drucker, and R. Kwok (2007), The areas and ice production of the western and central Ross Sea polynyas, 1991–2002, and their relation to the B-15 and C-19 iceberg events of 2000 and 2002, *J. Mar. Syst.*, *68*, doi:10.1016/j.jmarsys.2006.11.008.

Meier, W. N., M. Marquis, M. Kaminski, and R. Weaver (2004), NASA EOS sensors demonstrate potential for multiparameter studies of Arctic sea ice, *Eos*, *85*(46), 488–489.

Parkinson, C. L., D. J. Cavalieri, P. Gloersen, H. J. Zwally, and J. C. Comiso (1999), Variability of Arctic sea ice, 1978–1996, *J. Geophys. Res.*, *104*(C9), 20,837–20,856.

Steffen, K., and J. A. Maslanik (1988), Comparison of Nimbus 7 scanning multichannel microwave radiometer radiance and derived sea ice concentrations with Landsat imagery for the North Water area of Baffin Bay, *J. Geophys. Res.*, *93*(C9), 10,769–10,781.

Van Woert, M. L. (1999), Wintertime dynamics of the Terra Nova Bay polynya, *J. Geophys. Res.*, *104*(C4), 7753–7770.

Wensnahan, M., T. C. Grenfell, D. P. Winebrenner, and G. A. Maykut (1993), Observations and theoretical studies of microwave emissions from thin saline ice, *J. Geophys. Res.*, *98*(C5), 8531–8545.

Yu, Y., and D. A. Rothrock (1996), Thin ice thickness from satellite thermal imagery, *J. Geophys. Res.*, *101*(C11), 25,753–25,766.

_____

J. C. Comiso, Cryospheric Sciences Branch, NASA Goddard Space Flight Center, Code 614.1, Greenbelt, MD 20771, USA.

R. Drucker and S. Martin, School of Oceanography, University of Washington, Box 357940, Seattle, WA 98195-7940, USA.

R. Kwok, Jet Propulsion Laboratory, California Institute of Technology, 4800 Oak Grove Drive, Pasadena, CA 91109, USA.